Non-linear temperature dependence of nitrogen adsorption and decomposition on Fe(111) surface

Luigi Bonati*
Atomistic Simulations, Italian Institute of Technology, Genova, Italy

Daniela Polino
Department of Innovative Technologies, University of Applied Sciences and Arts of Southern Switzerland, Lugano, Switzerland

Cristina Pizzolitto, Pierdomenico Biasi
Basic Research, Research and Development Division, Casale SA, Lugano, Switzerland

Rene Eckert, Stephan Reitmeier
Clariant Produkte (Deutschland) GmbH, Bruckmühl, Germany

Robert Schlögl
Department of Inorganic Chemistry, Fritz-Haber Institute of the Max-Planck-Society, Berlin, Germany

Michele Parrinello†
Atomistic Simulations, Italian Institute of Technology, Genova, Italy

Abstract

The cleavage of the N_2 triple bond on the Fe(111) surface is believed to be the rate limiting step of the famed Haber-Bosch ammonia catalysis. Using a combination of machine learning potentials and advanced simulation techniques, we study this important catalytic step as a function of temperature. We find that at low temperatures our results agree with the well-established picture. However, if we increase the temperature to reach *operando* conditions the surface undergoes a global dynamical change and the step structure of the Fe(111) surface is destroyed. The catalytic sites, traditionally associated with the Fe(111) surface appear and disappear continuously. Our simulations illuminate the danger of extrapolating low-temperature results to *operando* conditions and indicate that the catalytic activity can only be inferred from calculations that take dynamics fully into account. More than that, they show that it is the transition to this highly fluctuating interfacial environment that drives the catalytic process.

The study of industrial catalysis is fraught with difficulties since it takes place in extreme conditions of temperature and pressure. So extreme in fact, that *operando* experiments become difficult, if not impossible. Experimental investigations have been limited to studying temperatures and pressures far below the industrial ones. Theoretical studies have also similarly assumed idealized conditions, possibly treating the dynamic effect as a perturbation. In the lack of other information, the *operando* behavior had to be inferred from the low-temperature low-pressure results. Only recently new technologies are providing access to *in situ* and *operando* characterization of catalytic materials, revealing the impact that such conditions have on their structure and corresponding activity [1]. Inspired by these findings, in this paper, we argue that at *operando* conditions major changes in the surface morphology and dynamics occur also at the atomic level rendering the extrapolation from low-temperature results of limited relevance.

To make this apparent, we study the dissociative chemisorption of N_2 on the Fe(111) surface. This is believed to be the rate-limiting step in the Haber-Bosch process for the production of ammonia and has been intensively studied. This is not surprising since ∼30% of the world's food is grown
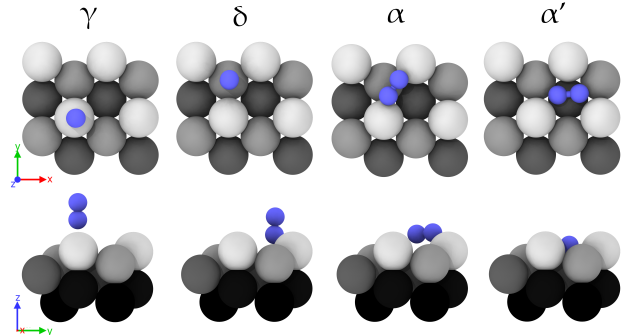

Figure 1: N_2 **adsorption sites on Fe(111)** from T=0 K calculations, top and side view. Iron atoms are colored as a function of the perpendicular z position.

using ammonia-derived fertilizers [2]. In addition, interest in ammonia synthesis has recently been rekindled in connection with the development of a hydrogen-based economy, as it could play an important role in storing hydrogen [3]. We refer the reader to the recent reviews and references therein for a complete overview of the process [4–6].

However, more than 100 years after its discovery, a full understanding of this catalytic process is still lacking. The Fe(111) crystal face is believed to be the most active, and as such it has been thoroughly investigated [7–23]. Ertl and coworkers [9, 11] have measured the variation of the absorbed N_2 bond vibration frequency. Their conclusion was that the absorbed molecules are oriented either perpendicular or parallel to the surface. This was supported by the theoretical work of Itoh *et. al.* [24], which showed that transferring charge from the 3d orbitals of Fe to the anti-bonding orbitals π^* of N_2 corresponds to a weakening of N-N bond different for the two geometries. This interpretation was later confirmed by Freund *et. al.* [14]. Later, Norskov and coworkers[17] performed static DFT calculations, confirming the scenario suggested by Ertl, but enriching it with new atomistic details. They distinguished between two different vertically absorbed N_2 sites (γ and δ) depending on whether the molecule sits on top of a first or second layer atom (Fig. 1). Similarly, there are two possible absorption sites when the molecule lies horizontally. In one, N_2 is in a bridge position between first layer atoms (α), while in the other it sits in a hollow position on top of an atom of the third layer(α'). The latter state is particularly relevant since it is believed to be the precursor to dissociation. According to Norskov such a state can be accessed either directly from the gas phase or via the sequence $\gamma \rightarrow \delta \rightarrow \alpha \rightarrow \alpha'$. In the α' site the molecule is in contact with seven-fold coordinated iron atoms (C_7) that can more easily donate electrons to the N_2 molecules, thus weakening the N-N triple bond. The higher activity of the (111) surface has been attributed to the step structure that stabilizes the α structure and the high density and easy accessibility of C_7 atoms in the open Fe(111) surface [25, 26]. Later on, we shall refer to the set of Fe atoms that surrounds the N_2 molecule in α' as the χ_7 cavity (represented below in the inset of Fig. 4). There are good reasons to look at this set of atoms as a catalytic site. Indeed, when the N_2 molecule moves towards the α' position the amount of charge transferred from the iron surface to the nitrogen molecule increases. Furthermore once inside the cavity, it can rotate between different equivalent orientations until the electronic orbitals are properly aligned for the reaction to take place.

Thanks to these classical experiments and calculations, it can be said that the low temperature behavior of N_2 on the Fe(111) surface is rather well understood. Unfortunately, neither experiments nor calculations are available in the *operando* range of temperature and pressures, *i.e.* T=700-850 K and P=100-200 bar. In this paper, we use modern molecular dynamical simulation methods to study the N_2 adsorption and cleavage as a function of temperature from the low ones to the *operando* regime. In so doing, we fully include entropy and dynamics effects.

A number of methodological innovations have made possible simulating such a challenging process. The first hurdle is that to study a catalytic process in which chemical bonds are broken and formed, the use of an *ab initio* approach is mandatory. However, due to their high computational cost *ab initio* simulations can only be carried out in small systems and for short simulation times. Realistic modeling instead, requires studying larger systems for longer times. A satisfactory compromise between accuracy and efficiency can be achieved if one follows the pioneering work of Behler and Parrinello[27] and trains a machine learning potential (MLP) to reproduce a suitably chosen set of quantum mechanical calculations. By combining these machine learning techniques with advanced sampling methods, this approach has been shown to reproduce well the potential energy surface of different reactive systems [28–37].

Although the use of ML potentials reduces the cost of *ab initio*-quality simulations by orders of magnitudes, these calculations are still too expensive and it is not possible to explore the time scales over which these reactive processes occur. However, combining them with state-of-the-art enhanced sampling methodologies allows the time scale problem to be circumvented. Here, we use the recently developed On-the-fly Probability Enhanced Sampling (OPES) method [38] which is an evolution of the widely used metadynamics technique [39, 40]. Once the simulations were completed, due to the observed high-temperature complex behavior new analysis methods were required to understand and describe the catalytic behavior. In particular, we monitor the charge transferred from the metal to the molecule. To this effect, we trained a second machine learning model that is able to predict charges without the need for expensive quantum mechanical calculations.

Armed with these tools, we study the N_2 adsorption and decomposition on the Fe(111) surface as a function of temperature. In particular, we find two contrasting behaviors. At low temperatures, the reaction proceeds as described in the literature. However, at higher temperatures, the surface atoms become highly mobile and the step structure of the surface is destroyed. Still, χ_7 cavities can be found but their number is reduced and have a finite lifetime, being continuously formed and broken. In addition, new catalytic sites are also formed. This alters both the adsorption free energy profile and the way the reaction proceeds. As a result, the high-temperature behavior cannot be inferred from the low-temperature one and the reaction proceeds in a way similar to that of a homogeneous catalytic process in which the mobile reagent reacts when it encounters the fluctuation of the environment that catalyzes the process. This highly mobile behavior is at odds with the standard picture that associates reactivity with well-defined static atomic arrangements.

Results

A reliable potential to study N_2 on Fe(111)

The first step of this work is the construction of a potential able to describe the properties of iron surfaces and their interaction with N_2 molecules during the adsorption and dissociation processes. To this effect, we trained a neural network-based potential on a set of single-point calculations so as to reproduce at best DFT energies and forces. For this procedure to be successful a careful choice of the training
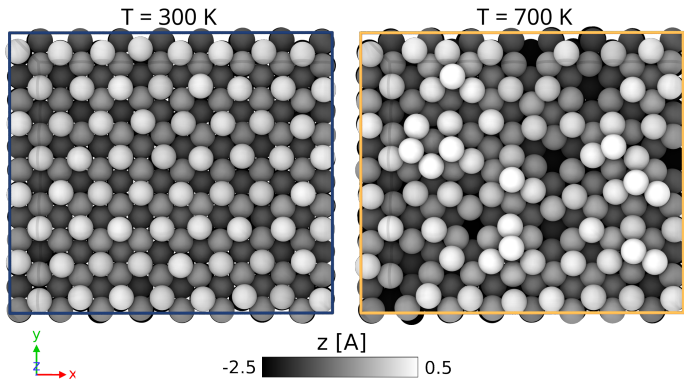
Figure 2: Fe(111) morphology: room temperature vs *in operando* condition. *Top view of final structures obtained from 20 ns molecular dynamics simulations of the Fe(111) at T=300K (left) and T=700K (right). Atoms are colored as a function of the Z position. Bright regions indicate adatoms, while dark regions the formation of vacancies on the surface.*

data set is needed, especially to model correctly the reactive pathways. Following our previous experience in modeling rare events with ML potentials [28, 31, 35], we collected configurations from a combination of enhanced and standard *ab initio* MD simulations followed by an active learning procedure (see Methods). A total of about 30k single-point DFT calculations were used in the training. Using the Deep Potential Molecular Dynamics [41, 42] scheme our potential obtains a mean absolute error (MAE) on energies of 0.60 meV/atom and on forces of 31 meV/A, while the Root Mean Squared Error (RMSE) is 0.81 meV/atom and 40 meV/A for energies and forces, respectively. In the Supporting Information (SI) we report the detailed composition of the dataset (Table S1) and extensive validation of the ML potential (Figs. S1-S3).

Temperature dependence of Fe surface morphology

Before studying the N_2 adsorption and the successive dissociation we find instructive to study the behavior of the pristine Fe(111) surface as a function of temperature. This study offers a number of surprises as evident from Fig. 2 where we compare two surface snapshots taken at T=300 K and T=700 K after 20 ns of MD simulations. The lower temperature structure is hardly distinguishable from the equilibrium one, instead, the higher temperature structure exhibits a considerable amount of disorder. The surface is no longer flat, the formation of hills and holes is clearly visible, and the ordered step structure of the (111) surface is lost. This reflects a very dynamic behavior as will become clear in the following.

We turn this initial impression into a quantitative study and follow how the surface changes as a function of temperature. In Fig. 3a we plot the temperature dependence of the density of surface exposed atoms along the (111) direction. In the low-temperature regime we observe only the expected thermal broadening. However, at temperatures above 500 K an adlayer is formed and the number of atoms in the first layer is depleted. This signals a very different behavior between a low-temperature regime $T < 500\ K$ and a higher-temperature one $T > 600\ K$. This is reflected in

the behavior of the surface roughness (Fig. 3b). The change in these two properties is accompanied by a different dynamical behavior as signaled by the increase in the diffusion coefficient of surface atoms. An analysis of the dynamics shows that the atoms in the first layers diffuse via jumps between different crystallographic positions (Fig. S4). Thus, in a grazing incidence diffraction experiment, Bragg peaks would still be measured, but the enhanced atomic motions would lead to a reduction of the Bragg peak intensities and in a broad diffuse background similar to what is observed in superionic conductors. At T=500 K the surface begins to disorder but since the diffusion coefficient is still low its disorder is basically static. However, at *operando* conditions surface dynamics is fully developed reaching liquid-like values. However revealing, the plots in Fig. 3 are unable to fully reflect the complex dynamics that takes place in the *operando* range of temperatures, and the reader is invited to vision the movies illustrating the dynamics (supplementary material). The surface looks like a stormy sea with local structures continuously being formed and broken.

So far our description has been based on standard surface physics analysis tools. However, our main interest is understanding how the dynamics influence surface reactivity. Thus, we study the temperature effect on the geometry of the cavities χ_7, which we recall are associated with the precursor α' state. To this effect, we use the similarity measure $\mathcal{S}(\chi, \chi_7)$ between the atomic environments $\{\chi\}$ of surface atoms and the χ_7 environment as defined in the methods section. By counting the number of surface atoms with an high similarity, we can identify the potentially active sites. From Fig. 4a it can be seen that at the *operando* temperatures the number of active sites decreases by about one-third as compared to the low temperature one. However, looking at the number of sites only gives a partial view of the phenomenon. To fully capture the behavior of the χ_7 sites we need to measure also their lifetime (Fig. 4b). In fact, the active sites are continuously created and destroyed with a lifetime distribution that is far from being Gaussian. As a consequence, the average values of the lifetime are not at all representative of the typical dynamics of χ_7 at high temperatures. In fact, the average lifetime is on the order of the tens of picoseconds, but the distributions have a tail that reaches the nanoseconds regime. Thus the reaction is still allowed to take place.

Nitrogen adsorption and dissociation mechanism

We now study the interaction of an incoming nitrogen molecule with the surface, its adsorption and subsequent splitting. To this effect we perform a set of OPES simulations enhancing the fluctuations of two distinct collective variables. One is the nitrogen-nitrogen interatomic distance $d(N, N)$, which is necessarily part of the reaction coordinate. The other is the coordination number between Fe and N atoms, which is meant to account for the geometric arrangement of the molecule relative to the surface, i.e. whether it is adsorbed and if so in which geometrical arrangement (see Methods).

While at low temperatures the adsorption geometries are easily identified (see Fig. 1), at high temperatures the continuous movement of surface atoms makes it difficult to
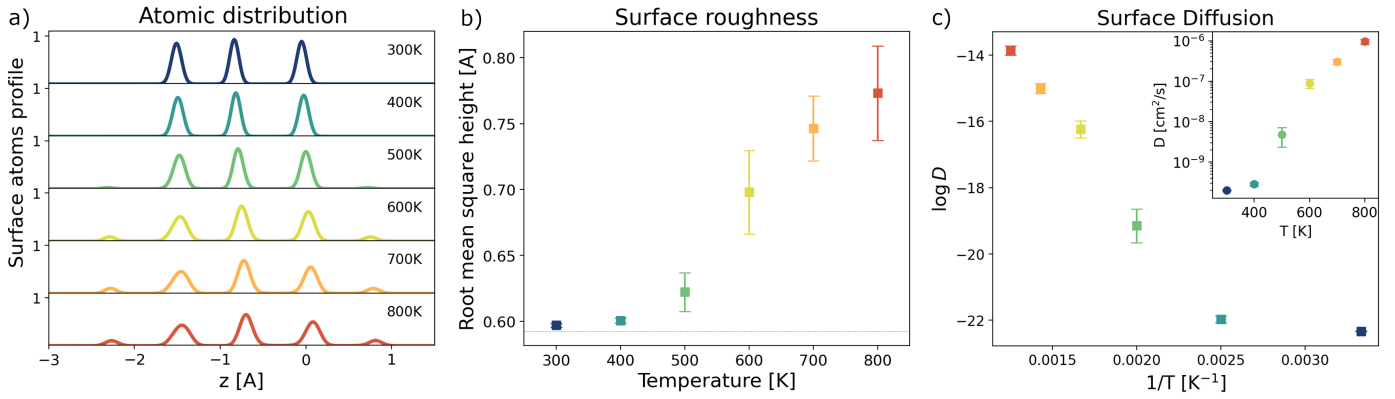
3

Figure 3: Fe(111) morphology and dynamics analysis as a function of temperature. *a) Atomic layer distribution of atoms belonging to the surface as a function of z. The emergence of new peaks at high temperatures denotes a roughening of the surface with the formation of adatoms (rightmost peak at 0.9 Å) and vacancies (leftmost peak at -2.2Å). The distribution is shown only for surface atoms dynamically identified at each time step by the Alpha-Shape method. b) Mean and standard deviation of the surface roughness measured as the standard deviation of the surface atoms' height. c) Logarithm of the diffusion coefficient of surface atoms as a function of inverse temperature (main panel) and diffusion vs temperature (inset).*

find a variable able to identify the N_2 pose. Previous experience [43] together with the findings of Itoh *et. al.* [24] have shown that the electronic structure is a very sensitive indicator of the atomic environment. For this reason, we monitor the charge q transferred from the metallic surface to the molecule. Partial charges are measured using the Bader electronic density decomposition [44, 45] and computed as the deviation of the Bader charges from their formal value. To be able to compute them in large systems, we trained a

Figure 4: Number and lifetime of χ_7 active sites. *(top) Average and standard deviation of the number of χ_7 sites exposed on the surface with respect to ideal surface. Inset: construction of reference environment χ_7 from the α' adsorption site. (bottom) Violin plot with the distribution of lifetimes of χ_7 sites. Line markers identify the average lifetime, while the width describes the distribution of the points.*

neural network on a set of DFT calculations (see Methods) to predict partial charges given only the atomic positions.

The resulting free energy surface (FES) is plotted in Fig. 5a for two contrasting temperatures as a function of the N-N distance d and the sum of the N charges $q = q(N_2)$. Let us begin by analyzing the low-temperature one, where we clearly find metastable states that are characterized by distinct N_2 charges. In the gas phase we have $q = 0$, but as soon as the molecule interacts with the surface the charge changes. Indeed, it goes from a low value ($q \approx 0.3$) when the molecule is adsorbed perpendicular to the surface, be it δ-like or in a γ-like vertical arrangement, to a medium value ($q \approx 1$) which corresponds to a α-like horizontal positions, and finally to the to a very high value ($q \approx 1.6$) where one can recognize the α' precursor state. This becomes apparent if we look at the T=300 K geometries in Fig. 5c, where atoms are colored on the basis of their charge. This allows us to monitor the underlying chemical changes. In particular, we observe how the charge transfer is asymmetrical between the two N atoms in the vertical states and symmetrical in the horizontal ones. The vertical adsorption states identified by calculations at T=0 K (γ and δ) are characterized by the same charge transfer. To resolve them, it is necessary to project the free energy along the distance of N2 from the surface (Fig. S6). There we see how, over the entire temperature range, the free energy barrier between the two is so small that they can be considered as part of the same metastable state.

From the free energies, we can state that the only possible path to reach the precursor α' state is to pass first a vertical position and then a horizontal one. Furthermore, we observe that the increase in charge transfer is accompanied by a weakening of the N-N bond, as discussed by Ertl and collaborators [7, 24]. If we focus on the dissociation barrier, we see that beyond the high charge basins, a narrow tube leads the transition state which is located at values $q \approx 2$ and $r \approx 1.7$ which are highly consistent with the chemistry of the process.
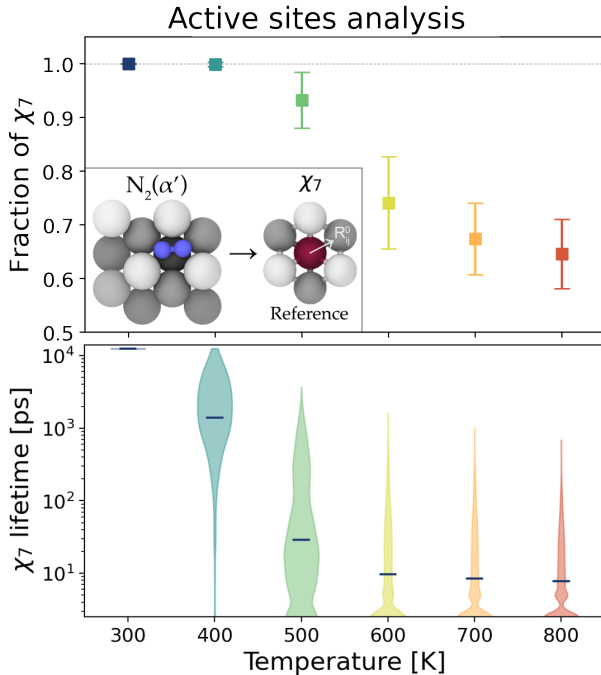
If we analyze the free energy surface at high-temperature we find that the shape is about the same, with similar metastable states as a function of charge and distance, albeit less defined. However, there is no longer a correspondence between free energy minima and classical adsorption states. As can be seen from the snapshots of T=700 K geometries shown in Fig. 5c, the metastable states now correspond to an ensemble of mostly disordered and defected structures. Consequently, if we set out to enumerate all the minima of potential energy we would find countless geometrically distinct states. Using the charge q as a collective variable allows us to group all geometrically different configurations according to their ability to weaken the N-N bond, which is the driving force of the process.

We have computed similar two-dimensional free energy plots in the range of temperature from 300 to 800 K (Fig. S7). To make a detailed comparison between all these free energies it is better to make a one-dimensional projection along the minimum free energy paths. Remarkably these pathways can all be superimposed in the (d, q) plane (Fig. S8) in spite of the different underlying dynamical behavior. In Fig. 5b all these free energy curves are aligned to the α state minimum and we see once again a strong difference in behavior between low and high temperature (see also Fig. S9). The low-temperature behavior is essentially the one predicted by Norskov and collaborators modulo the merging together of γ and δ states. Notably, the free energy barrier between the α state and the dissociated one is close to the one obtained from static DFT calculations [17, 21, 23, 46]. However, if we raise the temperature above 500 K things change dramatically, and α' is now but an imperceptible shoulder. This is an important deviation since the α' state is considered the precursor state to dissociation. This is mostly due to the temperature-induced disruption of the χ_7 cavities discussed earlier. As a consequence, the free energy barrier dividing the N_2 states from $2N$ becomes larger in the high-temperature regime (Fig. S9).

To deepen our analysis on the fate of the α' site we computed the distribution of the similarity $S(\chi_{N_2}, \chi_7)$ between the environment of the Fe atom that sits below the N_2 (see Methods) and the reactive χ_7 reference one. We restricted this analysis to the high-charge (precursor) region by selecting only configurations with $q > 1.35\ e$. At room temperature the distribution peaks at values close to 1, which means that N_2 is effectively adsorbed inside the χ_7 environment (i.e. α' state), see Fig. 6 top panel. In contrast, at T=700 K, the distribution peaks at smaller values, not compatible with the traditional site, and only a small shoulder is associated with the χ_7 site. Thus, at T=700 K the probability of being adsorbed in the χ_7 cavity is highly suppressed relative to room temperature. In particular, this reduction is greater than the decrease in the number of active sites alone reported in Fig. 4. This reinforces our argument that at high temperature we cannot rely on the correspondence with local minima of potential energy at T=0 K, as surface dynamics leads to dramatic distortion of adsorption configurations.

We then study the nature of the states that pertain to the transition region for N_2 dissociation. For each temperature, we performed a committor analysis on a subset of configurations extracted around the maxima of the mini-
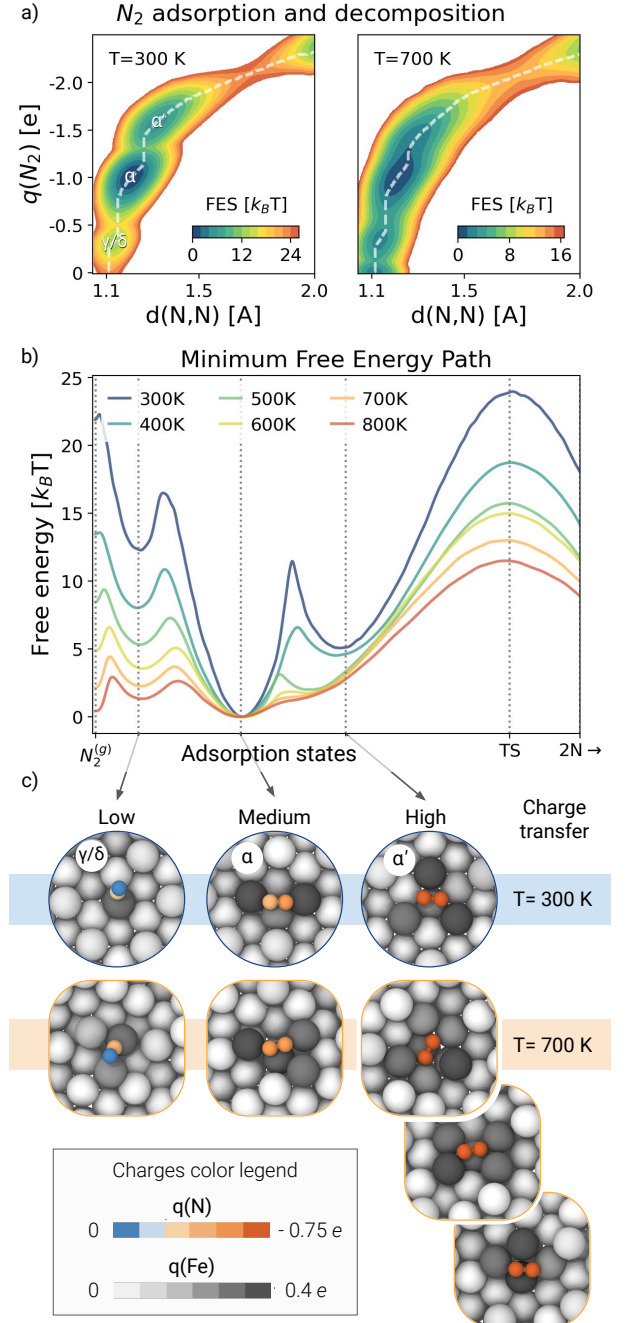

Figure 5: Adsorption and decomposition mechanism. *(a) Free energy as a function of N-N distance and the N_2 partial charge. Local minima represent the metastable states, and white dashed lines denote the minimum free energy pathways in this plane. (b) Free energy calculated along the minimum free energy pathways in the $d - q$ space, from the gas phase ($N_2^{(g)}$) to the adsorption states to the dissociated state ($2N$). The free energy at each temperature is rescaled by the thermal energy $k_B T$, where k_B is the Boltzmann constant. See Fig. S9 for the free energy in energy units. Free energies are shown only up to an N-N distance of 2 Å, from which a harmonic restraint is applied. (c) Snapshots of representative geometries of the adsorption states based on the amount of charge transferred for T=300K and T=700K. Atoms are colored according to charges predicted by the neural network model.*

mum free energy pathways (see Methods). This allows for identifying an ensemble of transition state configurations, defined as atomic realizations for which the probability to go into the reactant or in the product states is similar. If we plot the histogram of these configurations as a function of q the resulting distribution is centered around the $q \approx 2$ value at all temperatures (see Fig. S10). This is a reassuringly meaningful value since the transfer of two electrons is needed to break the N_2 triple bond. In the bottom panel of Fig. 6 we report the distribution of transition states' similarity with the χ_7 arrangement for T=300 and T=700 K. At low temperature the reactive configurations are only of the χ_7 type while at the higher temperature a number of new atomic arrangements capable of transferring two electrons to the dissociating molecule are activated by the dynamical roughening of the surface. A sample of such nonstandard active sites can be found in the SI (Fig. S11). However, even in this second regime the distribution remains peaked at a value compatible with the χ_7 state, unlike in the analysis of configurations characterized by high charge. This tells us that although the dynamics of surface atoms significantly suppresses the α' state, the formation of the cavity remains crucial for nitrogen decomposition. We can describe it as the eye of the needle through which the N_2 must pass to break the bond. However, the manner in which the molecule arrives in this state is strongly influenced by surface dynamics, and cannot be properly accounted for by approaches based on static calculations at T=0 K or perturbations thereof.

Conclusions

Dynamics has a disruptive effect on the morphology of the Fe (111) surface, with great consequences on the adsorption and dissociation of nitrogen molecules. This results in a drastic change in the behavior of the catalyst when going from low to high temperature, a change that takes place in a highly nonlinear way. This shows the danger of extrapolating high-temperature behavior from low-temperature experiments or theories.

More generally, our work puts into question a static approach to catalysis, especially the industrial one. It is not a static atomic arrangement that induces catalysis, but catalytic sites are continuously formed and disrupted. While this may seem detrimental at first, the structural dynamics of the surface could have an overall beneficial effect on catalytic performance. For the specific case of ammonia synthesis, the transient existence of the dissociation site for nitrogen might prevent the resulting reactive species to form a stable nitride [47] thus poisoning the catalyst. Likewise, any co-adsorbate that hinders the dynamic rearrangement of the iron surface, will act as potent poison; the extreme sensitivity of the catalysts [48] against oxygen, water, or sulphur species reducing the performance at concentrations way below the onset of phase formation as oxide or sulphide find so their functional explanation. The detailed analysis of the charge re-distribution between iron and nitrogen presented here defines a successful ammonia synthesis catalyst to be bi-functional. As potent as the high availability of negative charge is for the reductive dissociation of dinitrogen, as much a different active site will be needed to allow bond formation between the resulting nitrido-ion with the hydride form of activated hydrogen being omnipresent
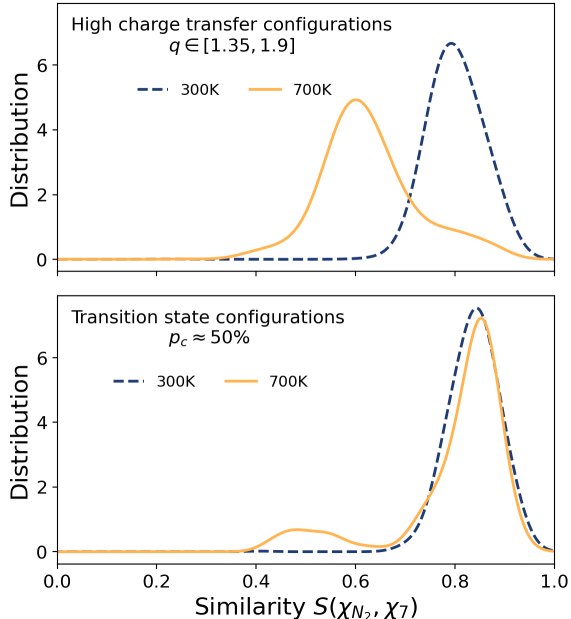
Precursor vs transition state configurations

Figure 6: High charge vs transition state configurations. *Distribution of the similarity between the neighborhood of the Fe atom on which N_2 is located and the χ_7 state for highly charged configurations (top) and for those in the transition state ensemble (bottom). They are computed with a Gaussian kernel density estimation, reweighted to reflect the equilibrium distribution (see Methods). All curves are normalized such that their integral sums to 1. Representative samples of the two peaks of the transition states (bottom figure) at T=700K are reported in the SI (Fig. S11).*

on the catalyst surface. This request may explain part [49] of the crucial role of "promoters" that was found [50] experimentally. These promoters may function by forming nitride-metallate [51] intermediates allowing hydrogenation by partly anionic hydrogen species. The present work forms an excellent basis for elucidating optimal configurations of iron and its co-catalysts operating under realistic pressures and temperatures with gases of realistic chemical composition and opens a way towards circumventing the scaling relation barrier [52] limiting the performance of metal catalysts for ammonia synthesis.

Methods

DFT simulations. The database needed to train the ML potential consists of a set of *ab initio* molecular dynamics (AIMD) trajectories, as well as single-point calculations of configurations generated by the ML potential during the active learning procedure (see below). In both cases, simulations are performed using the PWscf code of Quantum ESPRESSO [53–55] supplemented by the PLUMED plugin [56] which is an open-source, community-developed library [57] for enhanced sampling calculations. The PBE [58] exchange-correlation functional is used. Ultrasoft RRKJ pseudopotentials [59] replace explicit core-valence electron interactions, while electron density and wavefunctions are expanded in plane waves with energy cutoffs of 640 and 80 Ry respectively. Occupation is treated by the cold smearing technique of Marzari *et al.* [60] with a Gaussian spreading of 0.04 Ry. Spin polarization is included to correctly describe the magnetic properties of iron. Convergence against cut-off energy, Monkhost–Pack sampling, and occupation was tested and the setup described was chosen as a compromise between feasibility and accuracy. Simulations were carried out with a time step of 1.0 fs in a constant volume and temperature (NVT) ensemble using the stochastic velocity rescaling thermostat [61]. In order to span a larger portion of the configurational space we simulated the systems at different temperatures ranging between 600 and 800 K. Slab models with 5,8,and 12 atomic layers (respectively 45, 72 and 108 atoms) are built, and a vacuum layer of at least 10 Å is set in the z-direction. The first two lowest Fe layers are kept fixed during optimization and molecular dynamics calculations. The Brillouin zone was sampled using a $2 \times 2 \times 1$ Monkhost–Pack k-point grid [62]. The same setup is adopted to analyze the cleavage of the N_2 bond on the Fe(111) surface. Enhanced sampling simulations are employed to speed up *ab initio* simulations and include configurations of adsorption/desorption events and especially of the cleavage of the N_2 bond (more details below).

Machine learning potential. We used the Deep Potential Molecular Dynamics Smooth Edition scheme [41, 42] as implemented in the DeePMD-kit software [63]. The energy is decomposed as a sum of atomic contributions that depend on local environments within a cut-off range. Two different networks are used, one for embedding the atomic positions into symmetry invariant descriptors and the other for the regression task. The embedding network has three hidden layers and [30, 60, 120] nodes per layer, with an embedding matrix size of 20. The fitting network has three hidden layers and [240,240,240] nodes per layer. The cutoff radius was set to 6.0 Å with a switching function that decays from 5.7 Å to ensure continuity. The learning rate decays from 0.001 to $3.5 \cdot 10^{-8}$ with a decay constant of 4 epochs. The loss function used is a weighted root mean square error (RMSE) on energy and forces, with prefactors varying during training from 0.02 to 1 for energy and from 1000 to 1 for forces. The potentials used during the active learning phase are trained for 200 epochs, while the final one is trained for 800 epochs. The database is divided into training, validation, and test (80-15-5%). Four different models are trained on different permutations of the training and validation databases, while the test portion is used only to assess the accuracy of the model at the end of the fitting procedure.

After training an initial model on AIMD data, an active learning strategy is used. The standard deviation of the predictions given by the ensemble of 4 NN models is used as a proxy for uncertainty. Then, standard molecular dynamics simulations and advanced sampling simulations are performed to collect new configurations. To minimize the number of costly single-point DFT calculations, only configurations for which the standard deviation of a force component is greater than 200 meV/A are considered. The use of advanced sampling simulations is critical at this stage, as it allows the collection of configurations not only from the local minima but along all the reactive pathways.

Molecular dynamics simulations. Classical molecular dynamics simulations were performed with Large-scale Atomic/Molecular Massively Parallel Simulator (LAMMPS) software [64], patched with DeepMD-kit 2.1 [63] and PLUMED [56]. NVT simulations were performed with an integration time step of 0.5 fs. The temperature was controlled using stochastic velocity scaling thermostat [61] with a coupling constant of 100 fs.

During the active learning phase, simulations of small systems were performed with a $3 \times 3 \times N_l$ slab and N_l is the number of layers equal to 5, 8 or 12, such that their energy and forces can be computed with DFT calculations. When the potential is optimized, simulations lasting 20 ns were performed with an $8 \times 8 \times 12$ slab corresponding to 768 Fe atoms together with an N_2 molecule for the adsorption/dissociation simulations. In all simulations, the bottom two layers were fixed to impose a boundary condition that mimics a semi-infinite slab. Periodic boundary conditions were applied in the x- and y-directions, while along z a reflecting wall was applied above the surface. The distance of the wall from the top layer of the surface depends on the temperature and is such that a partial pressure of N_2 equal to 10 bar, according to the equation of state for ideal gases, is maintained.

Surface analysis. To analyze the morphology and dynamics of the iron surface, we first apply the Alpha-Shape method [65], as implemented in OVITO [66], to reconstruct the surface from the atomic positions. This method constructs a three-dimensional surface mesh using a virtual sphere to identify the surface separating the accessible volume (void) from the inaccessible volume (slab). The radius of the sphere used is equal to 2 Å. This makes it possible to identify the atoms that belong to the surface at each time step and limit the subsequent analysis to these, even if they change over time as is the case here due to high mobility.

Surface roughness is calculated as the standard deviation of the heights of the atoms on the surface:

$$S_q(t) = \sqrt{\frac{1}{n} \sum_{i=1}^{N_s(t)} (z_i - \bar{z})^2} \tag{1}$$

where the sum runs over the $N_s(t)$ surface atoms identified by the Alpha-Shape method at time t.

The *diffusion coefficient* of surface atoms is computed from the time-lagged displacement as follows:

$$D = \frac{\langle (\mathbf{x}(t+\tau) - \mathbf{x}(t))^2 \rangle_{surf}}{2\tau} \qquad (2)$$

where the average is calculated only on surface atoms. In SI we show the dependence of the diffusion coefficient on the lag-time and its asymptotic convergence. Similar values can be extracted from the asymptotic behavior of the mean square displacement, however, we believe this method is better suited to the nature of diffusion, which occurs as jumps between lattice sites.

Environment Similarity. To compare the environment around an atom with a reference, we use the environment similarity measure introduced by Piaggi and Parrinello [67]. This measure can be viewed as a non-rotationally invariant version of the popular SOAP (Smooth Overlap of Atomic Positions) kernel [68]. First, we define a smooth local density around the central atom by fitting a Gaussian to the position of each neighbor i:

$$\rho_\chi(\mathbf{r}) = \sum_{i \in \chi} \exp\left(-\frac{|\mathbf{r}_i - \mathbf{r}|^2}{2\sigma^2}\right). \qquad (3)$$

Here σ is a broadening parameter and $\mathbf{r_i}$ the position of atom i with respect to the central atom. We then define the environment similarity between χ and a reference χ_{ref} as:

$$S(\chi, \chi_{ref}) = \int d\mathbf{r} \rho_\chi(\mathbf{r}) \rho_{\chi_{ref}}(\mathbf{r}) \qquad (4)$$

which becomes:

$$S(\chi, \chi_{ref}) = \frac{1}{n} \sum_{i \in \chi} \sum_{j \in \chi_{ref}} \exp\left(-\frac{|\mathbf{r}_i - \mathbf{r}_j^0|^2}{4\sigma^2}\right) \qquad (5)$$

once we perform integration and we normalize the kernel such that $S(\chi_{ref}, \chi_{ref}) = 1$. Here n represents the number of atoms in the environment χ_{ref}.

The environment chosen here as reference for the analysis of active sites is the χ_7 environment defined in Fig. 4. This is the environment of a surface atom of the third layer corresponding to the cavity in which the N_2 is adsorbed in the α' state, surrounded by 7-coordinated Fe atoms. As for the computational parameters, we included all Fe neighbors up to 3.5 Å for constructing the local density. To remove thermal fluctuations, we first performed a moving average of the atomic positions with a window of 2.5 ps. Furthermore, we used different values of the broadening parameter σ depending on the simulation temperature. Specifically, we used $\sigma = 0.15$ for $T \leq 500$ K, $\sigma = 0.17$ for $T = 600$, $\sigma = 0.185$ for $T = 700$ and $\sigma = 0.2$ for $T = 800$ K. These numbers were chosen so that the position of the peak of χ_7 atoms is approximately the same for the ideal case (i.e., for a surface with only thermal fluctuations and no observed diffusion, see the dashed lines in Fig. S5).

Once we have calculated the environment similarity for each atom on the surface, we define the sites χ_7 as those environments that have $S(\chi, \chi_7) \geq 0.8$. The choice of the threshold value is based on the minima of the ideal distribution of environment similarity at each temperature (Fig. S5) where the ideal environments are defined above.

Neural network charge model. In order to predict the atomic charges from the atomic positions generated by the MLP-based molecular dynamics, we fitted a second neural network on a data set of charges computed with DFT. This allows us to predict the charges given only the atomic positions and the chemical species. To extract the charges from the electron charge density, we used the Bader decomposition scheme [44, 45] to compute the number of valence electrons. Then, charges were defined as the deviation of Bader charges from their formal value. Here the reference values were taken to be equal to 8 e and 5 e for Fe and N atoms, respectively. The charges were computed for a subset of configurations taken from those used to train the potential, for a total of about 10k configurations, which were split into training and validation set (80-20%).

To fit the charges, we used the deep tensor neural network SchNet architecture [69], which was proposed for fitting ML potentials, as implemented in the SchNetPack library [70]. To represent the local atomic environment we used a SchNet module with 5 interaction layers, a 3.5 Å cosine cutoff with pairwise distances expanded on 30 Gaussians and 64 atomwise features and convolution filters. As for the output, we used an atom-wise module with 2 hidden layers and (64,64) nodes per layer. The loss function used was the mean square error between the predicted charges $\{q_i\}$ and the reference ones $\{q_i^{DFT}\}$:

$$\mathcal{L} = \frac{1}{N_{at}} \sum_i (q_i - q_i^{DFT})^2 \qquad (6)$$

We trained the NN using the optimizer Adam [71] and a learning rate of 0.001 with the early stopping criterion. The model obtained with these parameters has a Root Mean Square Error on the validation set equal to 10^{-4} e .

Enhanced sampling simulations. Even with the availability of a machine learning potential, many important processes such as chemical reactions continue to occur on time scales much longer than those accessible to standard molecular dynamic simulations. To enable these rare events to be simulated, numerous advanced sampling methods have been developed, and in particular one family of these is based on the so-called collective variables $\mathbf{s}(\mathbf{R})$ (CVs). The CVs are functions of the atomic coordinates R and are chosen to be the most difficult to sample modes of the system. Once they are identified, an external bias potential $V(s(R))$ is added to the system. The role of the bias is to enhance the s fluctuations and speed up their sampling. Thus, with an appropriate choice of s large energy barriers can be overcome so that rare events are accelerated and take place in an affordable computational time. In this work, we have used two such techniques: Metadynamics [39, 40] and the more recent OPES [38]. The bias potential was added to the MD engine via the PLUMED plugin [56], be it Quantum Espresso [53–55] or LAMMPS [64].

Metadynamics is a well-established method [39] in which a history-dependent bias potential $V(\mathbf{s}, t)$ is constructed as a sum of repulsive Gaussians centered at the visited points in the collective space. The effect is to discourage the system from visiting already explored configurations. In particular, we consider its Well-Tempered variant [40], where the height of the hills is decreased over time as a function of the already deposited bias with a rate that is

determined by the parameter γ. During the training data collection with *ab initio* simulations, we used well-tempered metadynamics to accelerate both adsorption and cleavage of the N_2 molecule on the Fe(111) surface. This allowed us to collect configurations along the reactive paths and teach the NN how to represent the potential along the chemical reaction. In these calculations, we used as CV the distance in the z direction between the N_2 center of mass and the bottom of the slab to accelerate N_2 adsorption, and the N-N distance to speed up N_2 dissociation. In both cases, a new Gaussian was deposited every 50 steps, with an initial height equal to 6 kJ/mol and a standard deviation equal to 0.04 Å, with a $\gamma = 30$.

OPES. In the second stage in which we studied the adsorption and decomposition of N_2 with the ML potential, we used the On-the-fly Probability Enhanced Sampling (OPES) method [38]. OPES is an evolution of metadynamics that converges faster and requires fewer hyperparameters to be chosen. It also allows limiting the amount of bias that is deposited to avoid exploring high free energy regions.[72] In this approach, rather than building on the fly the bias $V\big(s(R)\big)$, one reconstructs the equilibrium probability distribution $P(\mathbf{s})$ using a Gaussian Kernel density estimator (KDE). Given a preassigned target distribution $p^{tg}(\mathbf{s})$, the bias is then defined as:

$$V\left(\boldsymbol{s}\right) = -\frac{1}{\beta} \log \frac{p^{tg}(\boldsymbol{s})}{P(\boldsymbol{s})}. \tag{7}$$

At convergence $V\left(\boldsymbol{s}\right)$ drives the s distribution to the target $p^{tg}(\mathbf{s})$. The target distribution is chosen to be the well-tempered one: $p^{tg}(\mathbf{s}) \propto P(\mathbf{s})^{\frac{1}{\gamma}}$, in which the equilibrium distribution is broadened and the free energy barriers are lowered by a bias factor γ. OPES simulations for studying the adsorption and decomposition of N_2 used the N-N distance and iron-nitrogen coordination number as collective variables. We used the iron-nitrogen coordination number as a proxy for the charge transfer. Indeed, these two quantities are correlated, especially in the N_2 state. The coordination number is calculated in a continuous and differentiable manner as follows:

$$C_{N,Fe} = \sum_{i \in \{N\}} \sum_{j \in \{Fe\}} \frac{1 - \left(\frac{r_{ij}}{r_0}\right)^n}{1 - \left(\frac{r_{ij}}{r_0}\right)^m}. \tag{8}$$

The parameters used are $r_0 = 2.5$ Å, $n = 6$ and $m = 12$. The update of the OPES bias was performed every 1000 steps, with the initial width of the kernels equal to 0.025 for $d(N, N)$ and 0.25 for $C_{N,Fe}$. The barrier parameter was set to 80 kJ/mol. Note finally, that a harmonic restraint was applied at $d \geq 2$ Å with an elastic constant equal to 2000 kJ/mol/Å^2. This was to facilitate the reversible sampling of the adsorption states and the dissociation barrier, without the need to wait for the recombination to occur. Note that the equilibrium value of the N-N distance in the 2N state is greater than 2 Å and therefore it is not sampled.

Free energy calculations. At convergence, the free energy surface (FES) along the collective variables used for biasing can be recovered from the OPES simulation as:

$$F(\boldsymbol{s}) = -k_B T \log P(\boldsymbol{s}). \tag{9}$$

A more general way, which also allows the FES to be calculated along CVs other than those used for bias, is through a reweighting procedure [38]. When the bias is in a quasi-static regime, we can recover the expectation value of any quantity such as:

$$\langle O\left(\boldsymbol{R}\right)\rangle = \frac{\langle O\left(\boldsymbol{R}\right)\ e^{\beta V(\boldsymbol{s}(\boldsymbol{R}))}\rangle_V}{\langle e^{\beta V(\boldsymbol{s}(\boldsymbol{R}))}\rangle_V}. \tag{10}$$

In particular, if we are interested in the free energy profile along a given collective variable s we have $P(s) = \langle \delta(s - s(\mathbf{R})) \rangle$. To approximate $P(s)$ from the simulation data, we use a weighted Gaussian density estimator, with the weights corresponding to $w_t = e^{-\beta V(s_t)}$. For the calculation of the minimum free energy pathways from the two-dimensional FES we used the MEPSA (Minimum Energy Path Surface Analysis) package [73].

Committor analysis. To identify the transition state (TS) configurations, we selected a range around the dissociation barrier in the minimum free energy path and randomly chose within this range n configurations from the simulation trajectories at each temperature. For each of the selected configurations, m short MD simulations are started by initializing the velocities with a different random seed. The committor probability p_c, i.e., the probability of first committing to the dissociated $2N$ state rather than falling back into the N_2 state, is then monitored. Configurations that have a committor probability $p_c \approx 0.5$ are part of the transition state ensemble. In the practice, at each temperature studied we extracted $n = 500$ configurations and for each of them we tested the committor behavior running $m = 50$ unbiased simulation with different initial velocities. We classified as belonging to the transition state ensemble those configurations for which $0.25 \leq p_c \leq 0.75$. In such a way for each temperature we harness 100-150 transition state configurations for each temperature.

Visualization. OVITO [66] and Matplotlib [74] were used for producing the images.

Acknowledgments

Author contributions

All authors contributed to the study conception and design. D.P. performed the QM calculations, L.B. developed the methods, performed the simulations and analyzed data with help from all the authors, M.P. supervised all the steps of the project. L.B. and M.P wrote the first draft of the manuscript and all the authors edited and approved the final version.

* luigi.bonati@iit.it; † michele.parrinello@iit.it

References

[1] S. W. Chee, T. Lunkenbein, R. Schlögl, and B. R. Cuenya. "In situ and operando electron microscopy in heterogeneous catalysis—insights into multi-scale chemical dynamics". *Journal of Physics: Condensed Matter* 33 (2021).

[2] J. W. Erisman, M. A. Sutton, J. Galloway, Z. Klimont, and W. Winiwarter. "How a century of ammonia synthesis changed the world". *Nature Geoscience* 1 (2008).

[3] K. E. Lamb, M. D. Dolan, and D. F. Kennedy. "Ammonia for hydrogen storage; A review of catalytic ammonia decomposition and hydrogen separation and purification". *International Journal of Hydrogen Energy* 44 (2019).

[4] R. Schlögl. "Catalytic Synthesis of Ammonia—A "Never-Ending Story"?" *Angewandte Chemie International Edition* 42 (2003).

[5] H. Liu. "Ammonia synthesis catalyst 100 years: Practice, enlightenment and challenge". *Chinese journal of catalysis* 35 (2014).

[6] J. Humphreys, R. Lan, and S. Tao. "Development and Recent Progress on Ammonia Synthesis Catalysts for Haber–Bosch Process". *Advanced Energy and Sustainability Research* 2 (2021).

[7] G. Ertl, S. B. Lee, and M. Weiss. "Kinetics of nitrogen adsorption on Fe(111)". *Surface Science* 114 (1982).

[8] G. Ertl, S. B. Lee, and M. Weiss. "Adsorption of nitrogen on potassium promoted Fe(111) and (100) surfaces". *Surface Science* 114 (1982).

[9] M. Grunze et al. "π-Bonded N_2 on Fe(111): The Precursor for Dissociation". *Phys. Rev. Lett.* 53 (8 1984).

[10] G. Strasser, M. Grunze, and M. Golze. "Summary Abstract: The mechanism of nitrogen dissociation on Fe(111)". *Journal of Vacuum Science & Technology A: Vacuum, Surfaces, and Films* 3 (1985).

[11] M.-C. Tsai, U. Ship, I. Bassignana, J. Küppers, and G. Ertl. "A vibrational spectroscopy study on the interaction of N2 with clean and K-promoted Fe(111) surfaces: π-bonded dinitrogen as precursor for dissociation". *Surface Science* 155 (1985).

[12] M. Grunze, G. Strasser, and M. Golze. "Precursor mediated and direct adsorption of molecular nitrogen on Fe111". *Applied Physics A Solids and Surfaces* 44 (1987).

[13] C. T. Rettner and H. Stein. "Effect of vibrational energy on the dissociative chemisorption of N 2on Fe(111)". *The Journal of Chemical Physics* 87 (1987).

[14] H.-J. Freund et al. "The adsorption of N2 on Fe(111): Angle resolved photoemission and theoretical model studies". *Surface Science* 185 (1987).

[15] D. Strongin, J. Carrazza, S. R. Bare, and G. Somorjai. "The importance of C7 sites and surface roughness in the ammonia synthesis reaction over iron". *Journal of Catalysis* 103 (1987).

[16] D. R. Strongin and G. A. Somorjai. "On the rate enhancement of ammonia synthesis over iron single crystals by coadsorption of aluminum oxide with potassium". *Catalysis Letters* 1 (1988).

[17] J. Mortensen, L. Hansen, B. Hammer, and J. Nørskov. "Nitrogen Adsorption and Dissociation on Fe(111)". *Journal of Catalysis* 182 (1999).

[18] J. J. Mortensen et al. "Nitrogen adsorption on Fe(111), (100), and (110) surfaces". *Surface Science* 422 (1999).

[19] S. C. Yeo, S. S. Han, and H. M. Lee. "Adsorption, dissociation, penetration, and diffusion of N2 on and in bcc Fe: First-principles calculations". *Physical Chemistry Chemical Physics* 15 (2013).

[20] M. A. Nosir, L. Martin-Gondre, G. A. Bocan, and R. Díez Muiño. "Dissociative adsorption dynamics of nitrogen on a Fe(111) surface". *Physical Chemistry Chemical Physics* 19 (2017).

[21] J. Qian, Q. An, A. Fortunelli, R. J. Nielsen, and W. A. Goddard. "Reaction Mechanism and Kinetics for Ammonia Synthesis on the Fe(111) Surface". *Journal of the American Chemical Society* 140 (2018).

[22] H. Shi et al. "Quantum Effects in the Dissociative Chemisorption of N2 on Fe(111): Full-Dimensional Quantum Dynamics and Quasi-Classical Trajectory Study". *The Journal of Physical Chemistry C* 125 (2021).

[23] D. Liu, W. Zhao, and Q. Yuan. "Breaking the Linear Relation in the Dissociation of Nitrogen on Iron Surfaces". *ChemPhysChem* 23 (2022).

[24] H. Itoh, G. Ertl, and A. Kunz. "A molecular orbital study on the interaction of dinitrogen with transition metal atoms". *Chemical Physics* 59 (1981).

[25] N. D. Spencer, R. C. Schoonmaker, and G. A. Somorjai. "Iron single crystals as ammonia synthesis catalysts: Effect of surface structure on catalyst activity". *Journal of Catalysis* 74 (1982).

[26] G. A. Somorjai and N. Materer. "Surface structures in ammonia synthesis". *Topics in Catalysis* 1 (1994).

[27] J. Behler and M. Parrinello. "Generalized neural-network representation of high-dimensional potential-energy surfaces". *Physical Review Letters* 98 (2007).

[28] L. Bonati and M. Parrinello. "Silicon liquid structure and crystal nucleation from ab-initio deep Metadynamics". *Physical Review Letters* 121 (2018).

[29] N. Gerrits, K. Shakouri, J. Behler, and G.-J. Kroes. "Accurate Probabilities for Highly Activated Reaction of Polyatomic Molecules on Surfaces Using a High-Dimensional Neural Network Potential: CHD3 + Cu(111)". *The Journal of Physical Chemistry Letters* 10 (2019).

[30] M. F. Calegari Andrade, H.-Y. Ko, L. Zhang, R. Car, and A. Selloni. "Free energy of proton transfer at the water–TiO2 interface from ab initio deep potential molecular dynamics". *Chem. Sci.* 11 (9 2020).

[31] H. Niu, L. Bonati, P. M. Piaggi, and M. Parrinello. "Ab initio phase diagram and nucleation of gallium". *Nature Communications* 11 (2020).

[32] M. Galib and D. T. Limmer. "Reactive uptake of N_2O_5 by atmospheric aerosol is dominated by interfacial processes". *Science* 371 (2021).

[33] P. Li, X. Zeng, and Z. Li. "Understanding High-Temperature Chemical Reactions on Metal Surfaces: A Case Study on Equilibrium Concentration and Diffusivity of CxHy on a Cu(111) Surface". *JACS Au* 2 (2022).

[34] T. Devergne, T. Magrino, F. Pietrucci, and A. M. Saitta. "Combining Machine Learning Approaches and Accurate Ab Initio Enhanced Sampling Methods for Prebiotic Chemical Reactions in Solution". *Journal of Chemical Theory and Computation* 18 (2022).

[35] M. Yang, L. Bonati, D. Polino, and M. Parrinello. "Using metadynamics to build neural network potentials for reactive events: the case of urea decomposition in water". *Catalysis Today* 387 (2022).

[36] A. S. Raman and A. Selloni. "Modeling the Solvation and Acidity of Carboxylic Acids Using an Ab Initio Deep Neural Network Potential". *The Journal of Physical Chemistry A* 126 (2022).

[37] T. A. Young, T. Johnston-Wood, H. Zhang, and F. Duarte. "Reaction dynamics of Diels–Alder reactions from machine learned potentials". *Phys. Chem. Chem. Phys.* 24 (35 2022).

[38] M. Invernizzi and M. Parrinello. "Rethinking Metadynamics: From Bias Potentials to Probability Distributions". *Journal of Physical Chemistry Letters* 11 (2020).

[39] A. Laio and M. Parrinello. "Escaping free-energy minima". *Proceedings of the National Academy of Sciences* 99 (2002).

[40] A. Barducci, G. Bussi, and M. Parrinello. "Well-Tempered Metadynamics: A Smoothly Converging and Tunable Free-Energy Method". *Physical Review Letters* 100 (2008).

[41] L. Zhang, J. Han, H. Wang, R. Car, and E. Weinan. "Deep Potential Molecular Dynamics: A Scalable Model with the Accuracy of Quantum Mechanics". *Physical Review Letters* 120 (2018).

[42] L. Zhang et al. "End-to-end Symmetry Preserving Interatomic Potential Energy Model for Finite and Extended Systems". *arXiv* (2018).

[43] I. Stich, R. Car, and M. Parrinello. "Structural, bonding, dynamical, and electronic properties of liquid silicon: An ab-initio molecular-dynamics study". *Physical Review B* 44 (1991).

[44] R. F. Bader. "Atoms in molecules". *Accounts of Chemical Research* 18 (1985).

[45] G. Henkelman, A. Arnaldsson, and H. Jónsson. "A fast and robust algorithm for Bader decomposition of charge density". *Computational Materials Science* 36 (2006).

[46] Y. Y. Zhang, H. Niu, G. Piccini, D. Mendels, and M. Parrinello. "Improving collective variables: The case of crystallization". *Journal of Chemical Physics* 150 (2019).

[47] T. Kandemir, M. E. Schuster, A. Senyshyn, M. Behrens, and R. Schlögl. "The Haber–Bosch process revisited: on the real structure and stability of "ammonia iron" under working conditions". *Angewandte Chemie International Edition* 52 (2013).

[48] J. Folke, H. Song, J. Schittkowski, R. Schlögl, and H. Ruland. "Oxygen Poisoning in Laboratory Testing of Iron-Based Ammonia Synthesis Catalysts and its Potential Sources". *Chemie Ingenieur Technik* 92 (2020).

[49] J. Folke et al. "Promoter effect on the reduction behavior of wuestite-based catalysts for ammonia synthesis". *Catalysis Today* 387 (2022).

[50] D. Strongin, S. Bare, and G. Somorjai. "The effects of aluminum oxide in restructuring iron single crystal surfaces for ammonia synthesis". *Journal of Catalysis* 103 (1987).

[51] J. K. Bendyna, P. Höhn, and R. Kniep. "Crystal structure of tristrontium trinitridoferrate (III), Sr~ 3 [FeN~ 3]". *ZEITSCHRIFT FUR KRISTALLOGRAPHIE NEW CRYSTAL STRUCTURES* 223 (2008).

[52] A. Vojvodic et al. "Exploring the limits: A low-pressure, low-temperature Haber–Bosch process". *Chemical Physics Letters* 598 (2014).

[53] P. Giannozzi et al. "QUANTUM ESPRESSO: a modular and open-source software project for quantum simulations of materials". *J. Condens. Matter Phys.* 21 (2009).

[54] P. Giannozzi et al. "Advanced capabilities for materials modelling with Quantum ESPRESSO". *Journal of Physics: Condensed Matter* 29 (2017).

[55] P. Giannozzi et al. "Quantum ESPRESSO toward the exascale". *The Journal of Chemical Physics* 152 (2020).

[56] G. A. Tribello, M. Bonomi, D. Branduardi, C. Camilloni, and G. Bussi. "PLUMED 2: New feathers for an old bird". *Computer Physics Communications* 185 (2014).

[57] M. Bonomi et al. "Promoting transparency and reproducibility in enhanced molecular simulations". *Nature Methods* 16 (2019).

[58] J. P. Perdew, K. Burke, and M. Ernzerhof. "Generalized gradient approximation made simple". *Phys. Rev. Lett.* 77 (1996).

[59] A. M. Rappe, K. M. Rabe, E. Kaxiras, and J. Joannopoulos. "Optimized pseudopotentials". *Phys. Rev. B* 41 (1990).

[60] N. Marzari, D. Vanderbilt, A. D. Vita, and M. C. Payne. "Thermal Contraction and Disordering of the Al(110) Surface". *Phys. Rev. Lett.* 82 (16 1999).

[61] G. Bussi, D. Donadio, and M. Parrinello. "Canonical sampling through velocity rescaling". *J. Chem. Phys.* 126 (2007).

[62] H. J. Monkhorst and J. D. Pack. "Special points for Brillouin-zone integrations". *Phys. Rev. B* 13 (1976).

[63] H. Wang, L. Zhang, J. Han, and W. E. "DeePMD-kit: A deep learning package for many-body potential energy representation and molecular dynamics" (2017).

[64] S. Plimpton. "LAMMPS-large-scale atomic/molecular massively parallel simulator". *Sandia National Laboratories* (2007).

[65] A. Stukowski. "Computational Analysis Methods in Atomistic Modeling of Crystals". *JOM* 66 (2014).

[66] A. Stukowski. "Visualization and analysis of atomistic simulation data with OVITO-the Open Visualization Tool". *Modelling and Simulation in Materials Science and Engineering* 18 (2010).

[67] P. M. Piaggi and M. Parrinello. "Calculation of phase diagrams in the multithermal-multibaric ensemble". *Journal of Chemical Physics* 150 (2019).

[68] A. P. Bartók, R. Kondor, and G. Csányi. "On representing chemical environments". *PHYSICAL REVIEW B* 87 (2013).

[69] K. T. Schütt, H. E. Sauceda, P.-J. Kindermans, A. Tkatchenko, and K.-R. Müller. "Schnet–a deep learning architecture for molecules and materials". *The Journal of Chemical Physics* 148 (2018).

[70] K. Schütt et al. "SchNetPack: A deep learning toolbox for atomistic systems". *Journal of chemical theory and computation* 15 (2018).

[71] D. P. Kingma and J. Ba. "Adam: A method for stochastic optimization". *arXiv preprint arXiv:1412.6980* (2014).

[72] M. Invernizzi and M. Parrinello. "Exploration vs Convergence Speed in Adaptive-Bias Enhanced Sampling". *Journal of Chemical Theory and Computation* 18 (2022).

[73] I. Marcos-Alcalde, J. Setoain, J. I. Mendieta-Moreno, J. Mendieta, and P. Gómez-Puertas. "MEPSA: minimum energy pathway analysis for energy landscapes". *Bioinformatics* 31 (2015).

[74] J. D. Hunter. "Matplotlib: A 2D graphics environment". *Computing in Science & Engineering* 9 (2007).

SUPPORTING INFORMATION

Non-linear temperature dependence of nitrogen adsorption and decomposition on Fe(111) surface

Luigi Bonati [1], Daniela Polino, Cristina Pizzolitto, Pierdomenico Biasi,
Rene Eckert, Stephan Reitmeier, Robert Schlögl, and Michele Parrinello [2].

Validation of the machine learning potential

In Table S1 we report the composition of the dataset used for the ML potential fitting. We first checked the entire distribution of errors on the various systems (Fig. S1). Furthermore, to assess the reliability of the potential in generating new configurations, we compared the radial distribution function of Fe predicted by the MLP with that obtained from the DFT simulations (Fig. S2). Finally, we monitored the uncertainty of model predictions by calculating the standard deviation of an ensemble of MLPs on the configurations generated at different temperatures (Fig. S3).

Type	Formula	Training	Validation
AIMD	Fe45	4218	744
AIMD	Fe72	306	53
AIMD	Fe108	1465	258
AIMD	Fe45 N	1782	314
AIMD	Fe45 N2	2012	354
AIMD	Fe45 N4	1746	307
AIMD	Fe72 N	138	24
AIMD	Fe72 N2 H12	3496	616
AIMD	Fe72 N4 H20	1598	282
AIMD	Fe72 N6 H30	716	126
Active learning	Fe45	1128	198
Active learning	Fe72	336	59
Active learning	Fe108	1151	202
Active learning	Fe45 N	265	46
Active learning	Fe45 N2	5202	917
Active learning	Fe45 N4	272	48
Active learning	Fe72 N2	804	141
TOTAL		26635	4689

Table S1: Dataset for MLP construction. *Composition of the data set used for the fitting of the machine learning potential. A wide variety of systems were simulated: pure iron, with one or more nitrogen molecules and with nitrogen atoms, and - though not used in this study - also configurations with hydrogen. In all cases 5, 8, or 12 layers were simulated. Configurations were extracted every 2 or 5 fs from AIMD depending on whether they were metadynamics or standard MD simulations. As for the active learning part candidates were extracted every 1 ps and then selected based on the uncertainty on the predictions of a model ensemble.*

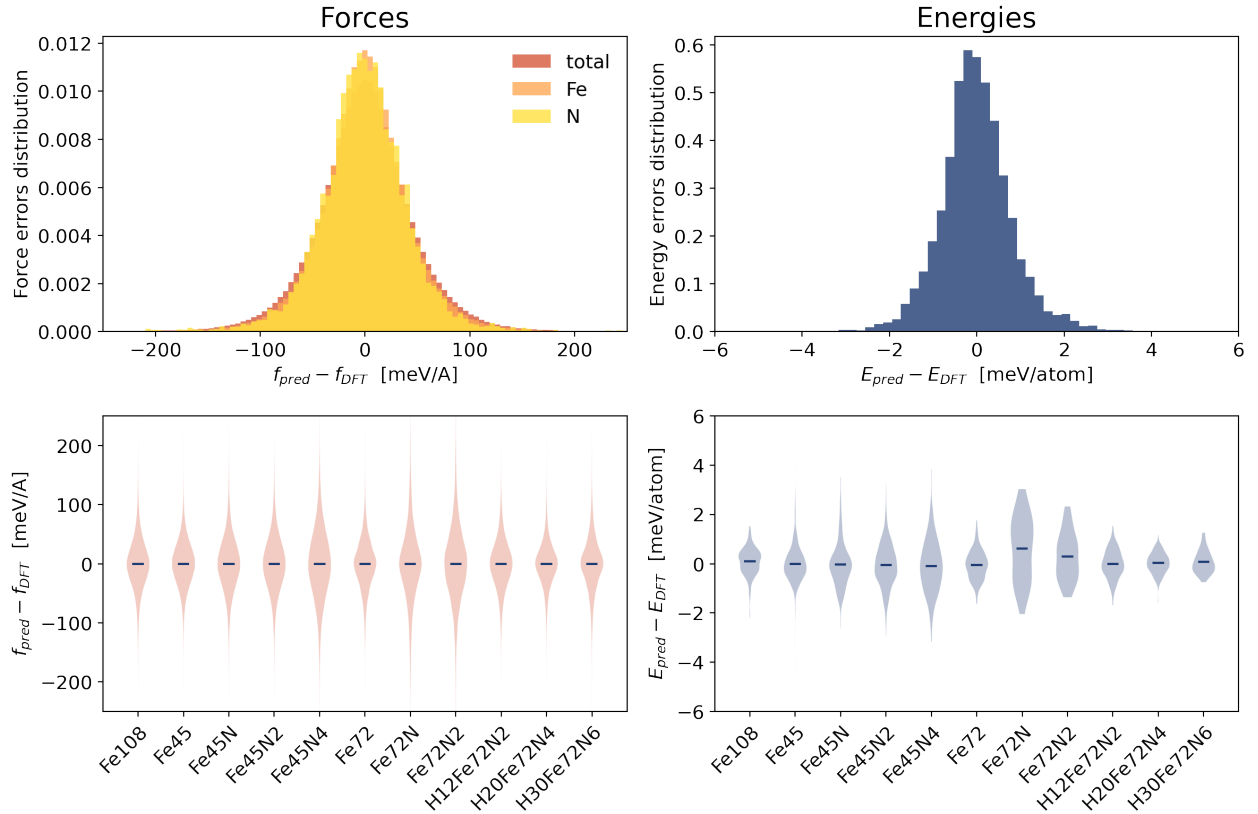[1]luigi.bonati@iit.it

[2]michele.parrinello@iit.it

Figure S1: Accuracy of energies and forces predictions on the test set. *The upper figures report the histogram of the errors on the forces (left) and energies (right) on the test set (corresponding to 5% of the final dataset ever used for training and validation of the ensemble of NN potentials). For the forces, the total distribution was reported along with the specific distributions of iron and nitrogen atoms, which are remarkably close. In the lower figures, we decomposed the error distributions for each system. The violin plot represents the error distributions on the forces (left) and energies (right) of the configurations grouped by chemical formula. The lines represent the mean value for each system.*
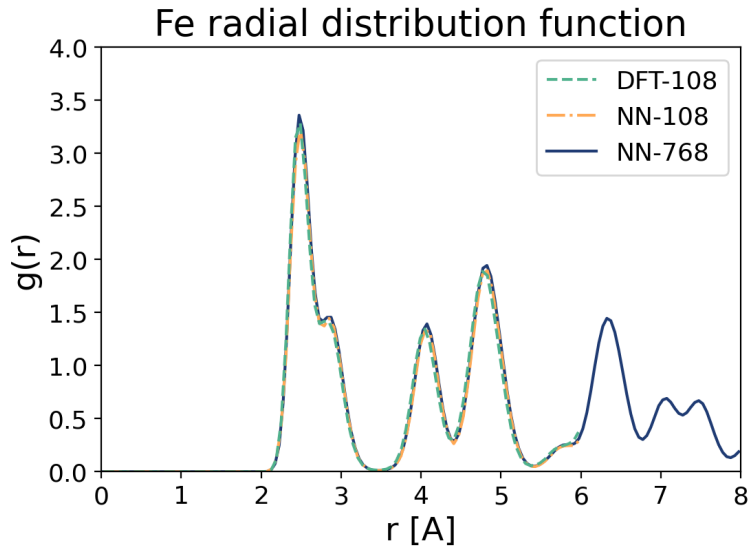
Figure S2: Fe radial distribution function. *Comparison of the $g(r)$ computed from DFT and from the machine learning potential. Two different simulations are performed, one with the same number of atoms of the DFT simulation (108 atoms) and one with a larger system (768 atoms). To make a fair comparison with the AIMD data, simulations of 10 ps were performed also with the MLP.*
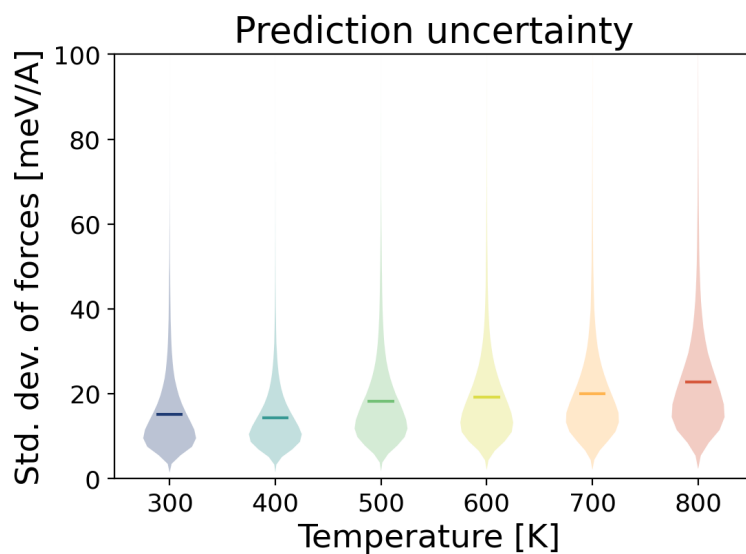
Figure S3: Uncertainty of force predictions over MD simulations. *Violin plot representing the distribution of the standard deviation of the force predictions for the configurations generated by the MLP in representative MD trajectories. The standard deviation is calculated from 4 MLPs trained on different permuations of training+validation dataset. This is then used as proxy for the uncertainty of the predictions. The lines denote the average values at each temperature.*

Additional results on Fe surface dynamics
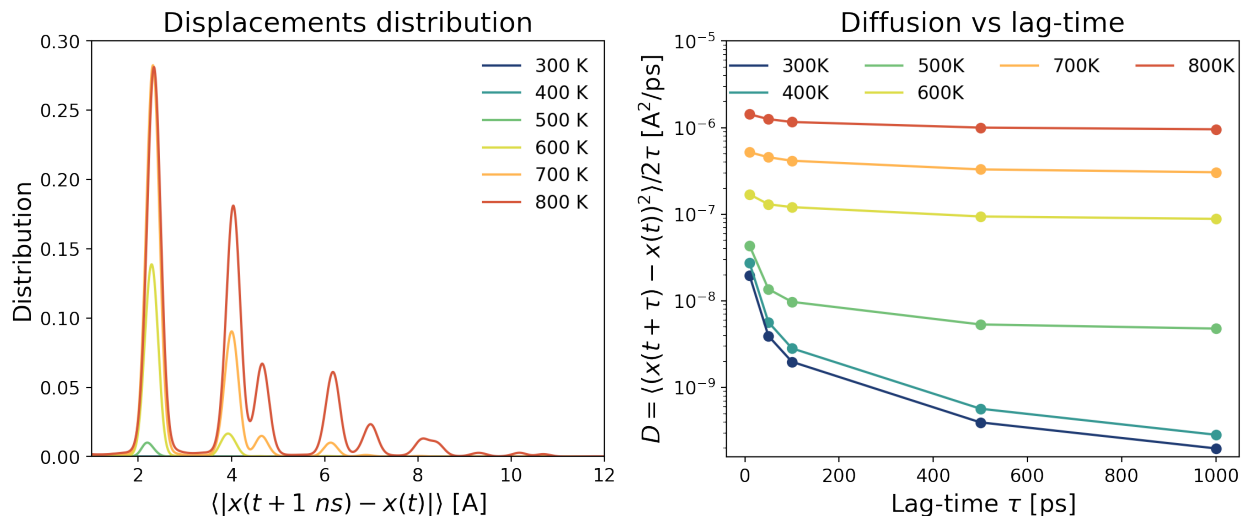
Figure S4: Surface diffusion additional analysis. *(left) Distribution of the time-lagged displacements of surface atoms with a lag time $\tau = 1$ ns. The peaks describe a jump diffusion between lattice sites rather than a liquid-like one. (right) Convergence of the diffusion coefficient computed from the average time-lagged displacements, as a function of the lag-time τ.*
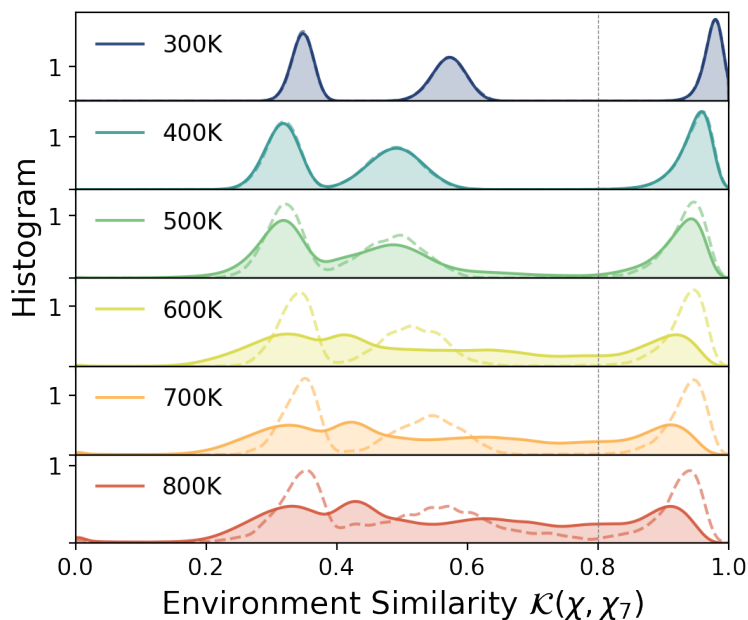
Figure S5: Environment Similarity distribution. *The histogram is calculated for the atoms in the surface for the equilibrated system (filled curves) and for the ideal surface accounting only for thermal fluctuations (calculated from the first 10 ps of the trajectory, checking that no diffusion of the surface atoms is observed). The threshold to decide whether a site is χ_7 or no is chosen to be equal to 0.8 (dotted vertical line), based on the minima of the ideal dashed curves.*

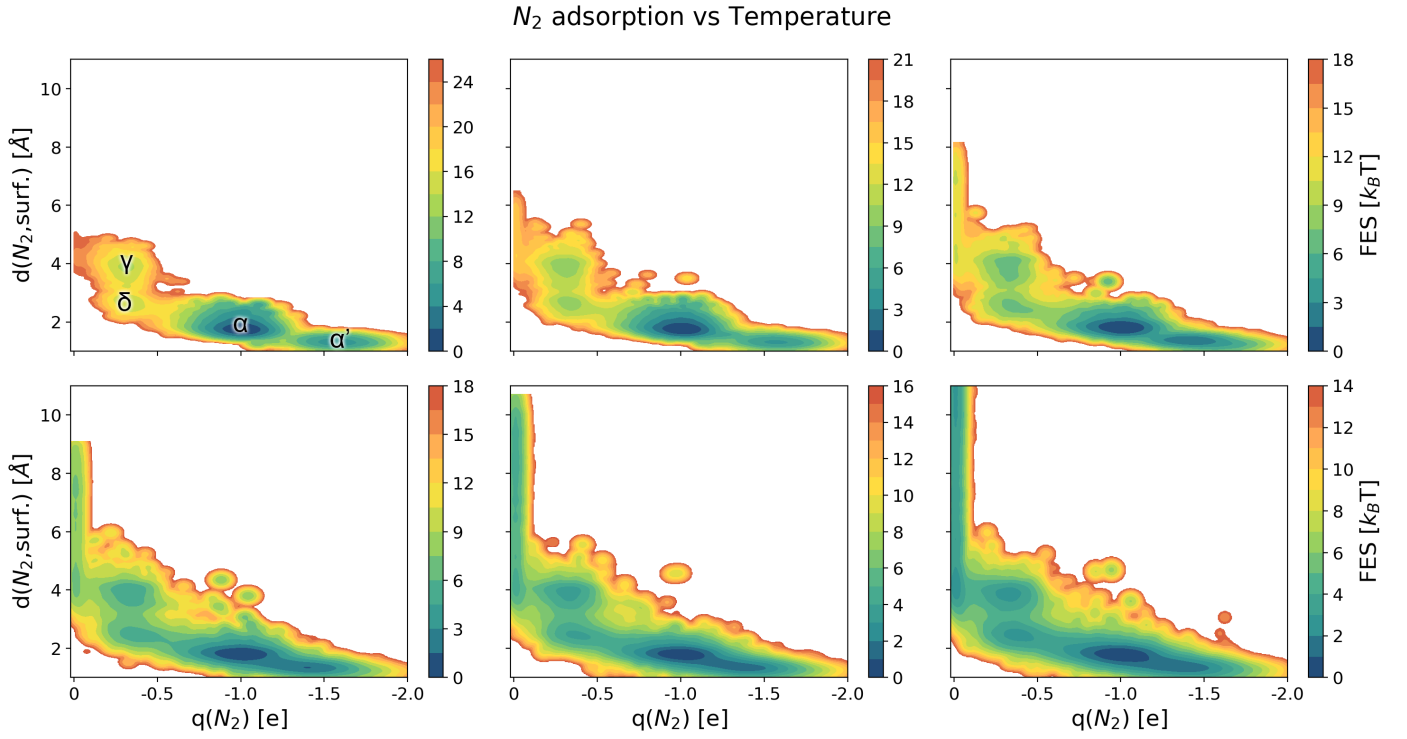## Additional results on N2 adsorption and dissociation

Figure S6: Adsorption mechanism vs temperature. Free energy profile of N_2 adsorption as a function of N_2 partial charge and the distance between N_2 center of mass and surface. To remove thermal fluctuations and to account for the roughening of the surface a two steps procedure is used to compute the distance between the surface and the moleucule. First, the trajectory is smoothed with a running average of the atomic positions of the Fe atoms. Then, a surface mesh is constructed with the Alpha-Shape method, and the distance from the center of mass of N_2 to the surface mesh. The two states around q=0.3 with different heights from the surface correspond to the N_2 molecule being adsorbed vertically on top of the first or the second layer (γ and δ sites).
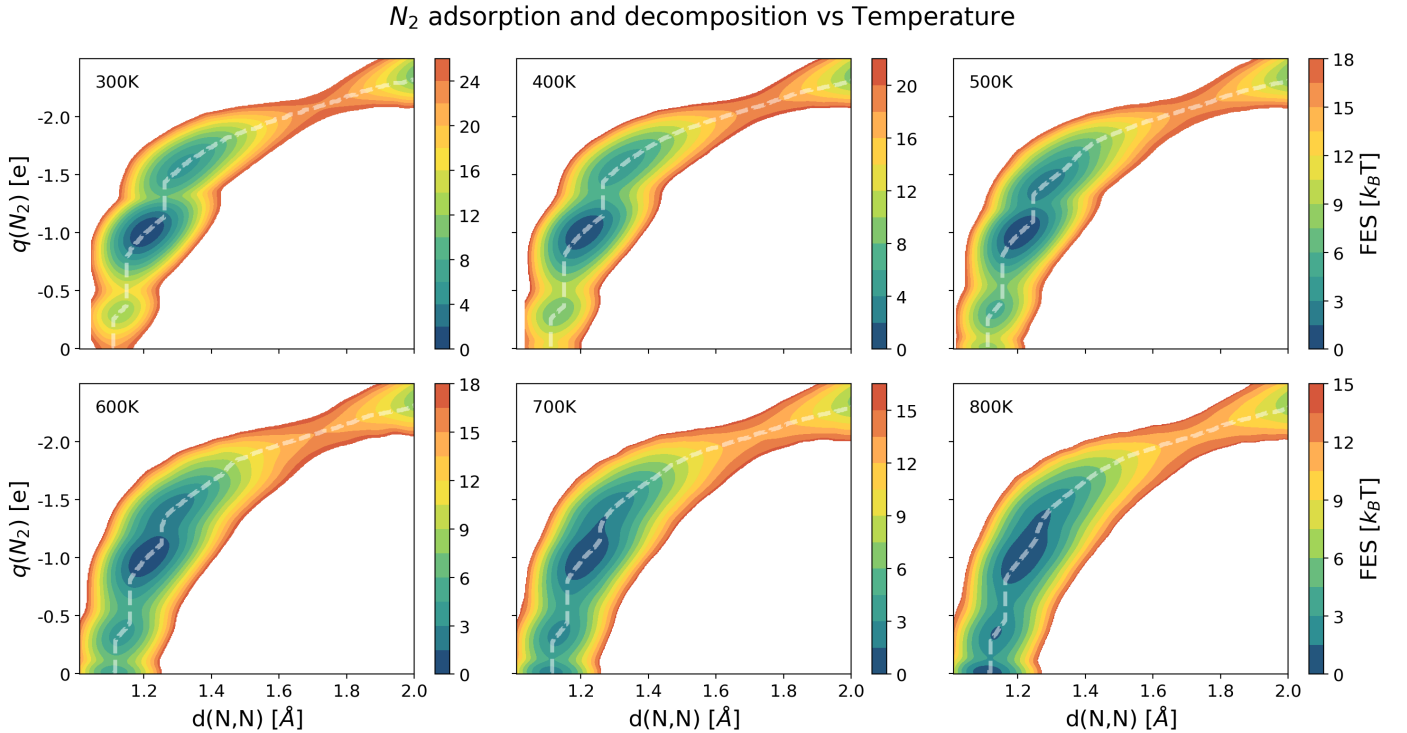

Figure S7: *N_2 decomposition mechanism. The free energy surface is computed as a function of N-N distance and N_2 charge for all the temperature range. White dashed lines denote the minimum free energy pathway.*
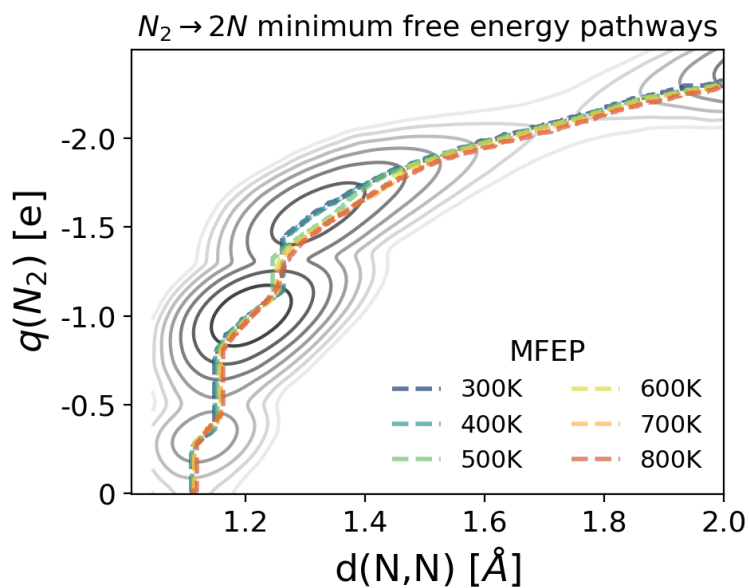
Figure S8: Decomposition pathways versus temperature. *The dashed lines represent the minimum free energy pathways calculated in the N-N distance and the $q(N_2)$ plane (dashed lines in Fig. S7), superimposed to the free energy at T=300K.*
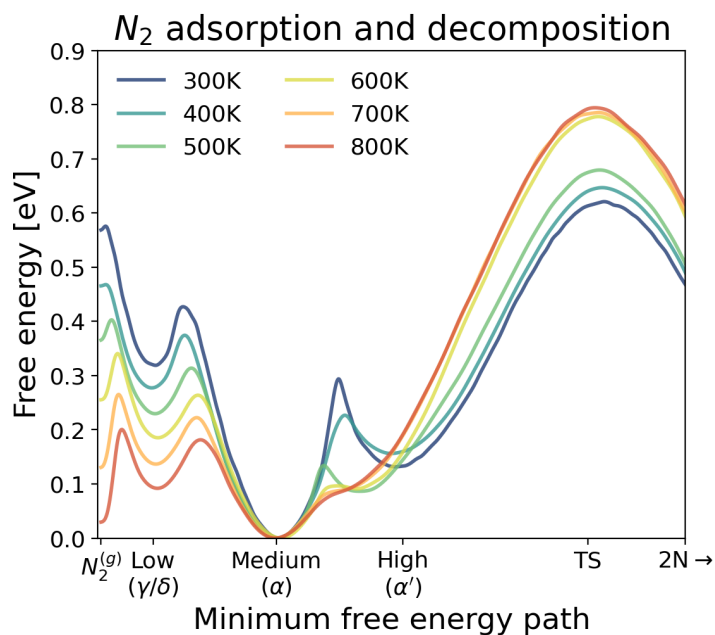

Figure S9: Adsorption and decomposition free energy profile. *Free energy along the minimum free energy pathways, as in Fig. 5 but in eV units rather than rescaling by thermal energy k_BT. Two different regimes are found, corresponding to the low and high temperatures.*
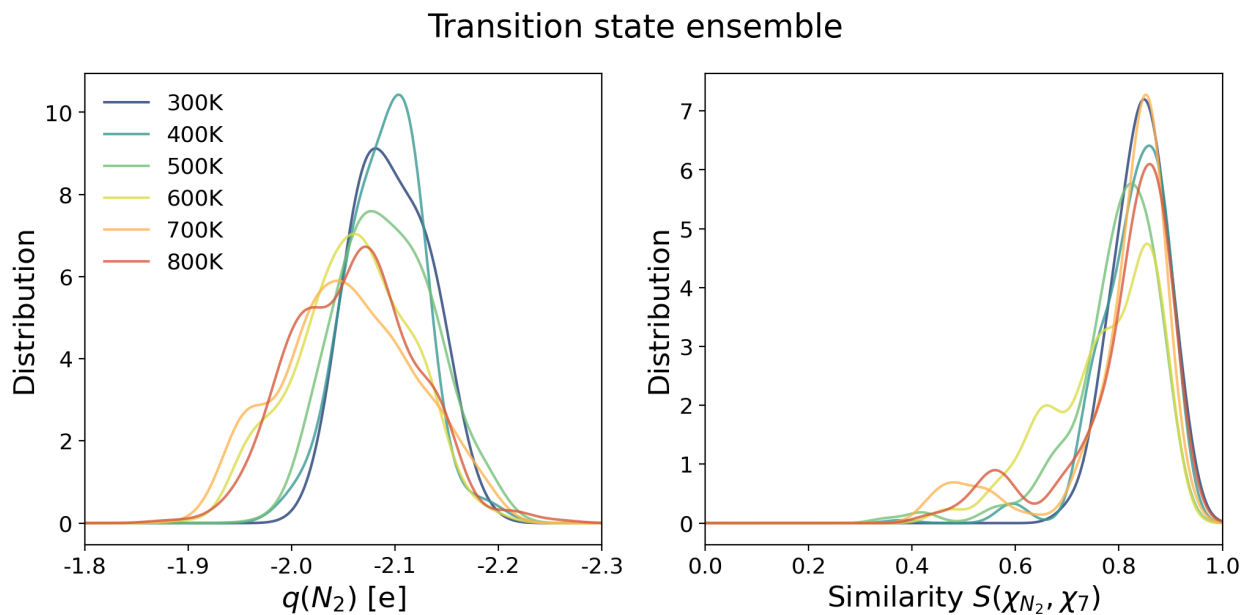
Transition state ensemble

Figure S10: Transition state ensemble. *Distribution of the N_2 charge (left) and environment similarity between the environment of the Iron below (right) for the transition state ensemble configurations selected from the committor analysis. The distributions are normalized such that their integral sums to 1.*
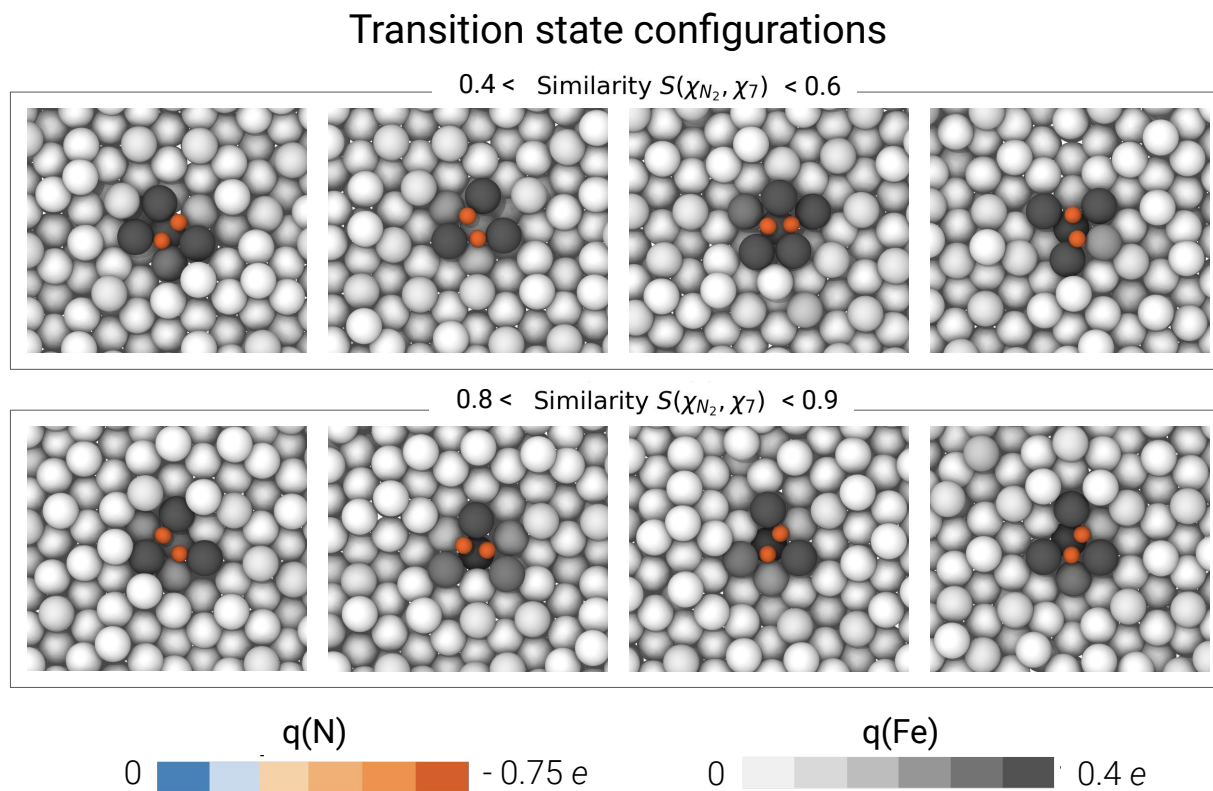
Transition state configurations

Figure S11: Transition state snapshots. *Configurations from the transition state ensemble at T=700K representative of the two peaks in Fig. 6b. Snapshots of configurations with low similarity (top row) and high similarity (bottom) between the environment of the Fe atom on which N_2 is located and the reference site χ_7. The top row contains samples of the highly disordered active sites created by the dynamical roughening of the surface. Within each group, the snapshots are ordered by increasing similarity measures.*